



Dynamical diffraction of an x-ray beam in a crystal of transiently population-inverted atoms

Dongyu Liu, Hankai Zhang

Supervisor: Andrei Benediktovitch

September 9, 2021

Abstract

We present simulations of diffractions from population-inverted crystals in the frame of the dynamical theory of x-ray diffraction. The developed approach is based on a numerical solution of modified time-dependent Takagi-Taupin equations and can be applied for modeling x-ray diffraction with crystals of arbitrary shape for the case of time-dependent susceptibility. We perform simulations for the propagation of the incident and diffracted waves. The amplitudes of the wave fields can be enhanced due to the population inversion. Based on our analytical calculations, we provide an interpretation on the amplification effect.

Contents

1	Introduction	3
2	Theory and numerical details	4
2.1	Population inversion	4
2.2	Time-dependent susceptibility	4
2.3	Time-dependent Takagi-Taupin equations	6
3	Results	9
3.1	The bench-marking calculations	9
3.2	The population-inverted diffraction	11
4	Summary	16

1 Introduction

X-rays provide a unique opportunity to obtain the structure of matter at atomic resolution. In crystals x-ray diffraction is successfully used over more than one hundred years to unravel the atomic and electronic structure with applications ranging from simple materials to large biological complexes. Despite the advent of novel, ultrabright x-ray sources, x-ray free-electron lasers (XFELs), the study of single particles of biological interest remains challenging. The challenge manifests itself in the inherently small elastic x-ray scattering strength which gives rise to diffraction. We are aimed to develop a novel imaging technique, relying on two-color pulses of XFELs. The first x-ray pulse will prepare atoms of the sample in core-excited states by promoting an electron of the inner-most electronic shell into a valence shell. The second x-ray pulse, tuned to an inner-shell transition, e.g. K-alpha transition, will elastically scatter on a set of atoms in states of population inversion. Two effects will enhance the scattering signal. On resonance, anomalous x-ray scattering gives an enhancement of the scattering strength. Moreover, scattering on core-inverted atoms can result in stimulated emission, that eventually gives rise to an exponentially enhanced signal amplification. The signal from population-inverted atoms can be analyzed together with non-resonant scattering from other atoms of the object, thus enhancing the contrast.

For most of the x-ray diffractive imaging experiments the dimensions of specimens are rather small, therefore the approximation of single-scattering, namely, the kinematical approximation is typically adopted. The kinematical theory provides a simple expression which allows us to calculate scattered amplitude from a finite size crystal as a Fourier transform of its electron density. Such simplification is not applicable for larger crystals, with the sizes bigger than the so-called extinction length, where effects of cross coupling between the diffracted and transmitted waves might become significant. These effects can be fully described in the frame of the dynamical theory which takes into account all multiple scattering effects. However, the dynamical theory provides no simple analytical expression for the scattering amplitude from a crystal of arbitrary shape. This theory has been extensively developed already for decades, but the influence of the dynamical effects on the results of diffraction for population-inverted medium has not yet been studied up to now.

As the fundamental exploration of the novel imaging technique, our aim is to study the role of multiple scattering, i.e., dynamical diffraction effects for scattering from population-inverted atoms. It will be instructive to identify the limits on the size of the objects below which the dynamical diffraction effect can be neglected, and kinematic diffraction can be used for analysis. When the diffraction can be analyzed in the kinematic theory, the structural analysis could be greatly simplified.

In this paper we present a numerical model based on modified time-dependent Takagi-Taupin equations for a general case of an arbitrary crystal shape to investigate the dynamical effects for diffraction from population-inverted medium. As the first stage of study, we simulate the population inversion of an inner-shell transition, i.e., the Mn $K\alpha_1$ transition, and calculate the x-ray susceptibility for the resonant probe light. Using the numerical model, we perform a series of simulations for the propagation of

the incident and diffracted waves in the population-inverted crystal. Next, we provide an interpretation on the amplification of the wave fields after its propagation in the crystal shown in the simulation results via analytical calculations. In this paper, we also demonstrate our method of correctness by reproducing the known numerical simulations.

2 Theory and numerical details

2.1 Population inversion

In order to prepare the population-inverted medium, we consider an x-ray free electron laser (XFEL) irradiating on a crystal sample. As a first approximation, we shall assume that the sample is small and the pump absorption is not essential. If the intensity of XFEL is strong enough, a large number of core-hole atoms will be produced. As a result, the population inversion will be established.

To investigate the response of the atoms to the intense x-ray radiation, we use the rate equation approach [1, 2]. It is easy to see this approach is phenomenological and captures the essential physics. The transitions among all possible electronic configurations $\{I\}$ of a given atom are described by a set of coupled rate equations of the form,

$$\frac{d}{dt}P_I(t) = \sum_{I' \neq I}^{\text{all config.}} [\Gamma_{I' \rightarrow I}P_{I'}(t) - \Gamma_{I \rightarrow I'}P_I(t)] \quad (1)$$

where P_I is the population of the I th configuration, and $\Gamma_{I \rightarrow I'}$ is the rate for transitions from configuration I to configuration I' . Here Γ can be either a time-independent Auger or fluorescence rate, or a time-dependent photoionization rate given by $\sigma_P j(t)$, where $j(t)$ is the photon flux of the x-ray pulse at a given time t . All configurations connected by the photoionization, Auger decay, and x-ray fluorescence processes are included in the calculation. The rate equations describe the dynamics of the atom, however, as the population inversion of a specific transition is what we are concerned with, we solely focus on the population of the two states related to the transition.

As an example, we consider the population inversion of the Mn $K\alpha 1$ transition. We obtain the populations of the states of Mn by using XATOM to calculate the rate equations, but as an output, we only need the populations of the two states, $1s^{-1}$ and $2p^{-1}$, that show population inversion as well as $K\alpha 1$ transition.

2.2 Time-dependent susceptibility

In population-inverted diffraction, an x-ray resonating to the specific transition with population inversion (e.g. the $K\alpha 1$ transition) is used as the probe field. The x-ray susceptibility due to the coupling to the resonant levels can be determined based on the distribution of population inversion calculated in Sec. 2.1.

We represent the single-color probe light as $\mathbf{E}_p = \mathbf{E}(\omega_p)e^{i\omega_p t}$, and the corresponding linear susceptibility is given by [3]

$$\overset{\leftrightarrow}{\chi}(\omega_p, t) = \frac{\mathcal{N}}{\varepsilon_0 \hbar} \sum_{n,m} [\rho_{mm}(t) - \rho_{nn}(t)] \frac{\boldsymbol{\mu}_{mn} \boldsymbol{\mu}_{nm}}{(\omega_{nm} + \omega_p) - i\gamma_{nm}} \quad (2)$$

which sums over all the possible states of the atomic system. In Eq. (2), \mathcal{N} denotes the atomic number density. ρ_{mm} is the population of level m , and ω_{nm} is the frequency of the $n \rightarrow m$ transition. $\boldsymbol{\mu}_{nm}$ and γ_{nm} is the transition dipole moment and the damping rate between level n and m , respectively. We see that the linear susceptibility is proportional to the population difference $\rho_{mm}(t) - \rho_{nn}(t)$ at time t , which provides the connection between population inversion and the susceptibility. For sake of simplicity, we can make the approximation that the susceptibility is a scalar. When the frequency of the probe light ω_p is close to one of the resonance frequencies of the atom, e.g. $-\omega_{nm}$, the frequency of $m \rightarrow n$ transition, (resonant to the Mn $K\alpha_1$ transition in our research), to good approximation the susceptibility is

$$\chi(\omega_p, t) = \frac{\mathcal{N}}{\varepsilon_0 \hbar} \frac{\mu_{mn} \mu_{nm}}{(\omega_{nm} + \omega_p) - i\gamma_{nm}} [\rho_{mm}(t) - \rho_{nn}(t)] \quad (3)$$

In general, the susceptibility in crystalline medium, which is a periodical function of the space coordinates, can be extended in a Fourier series [4]

$$\chi(\mathbf{r}) = \sum_{\mathbf{h}} \chi_{\mathbf{h}} \exp(-i\mathbf{h} \cdot \mathbf{r}) \quad (4)$$

where \mathbf{h} is a reciprocal lattice vector and the summation is extended over all reciprocal lattice vectors. The Fourier components can be calculated from

$$\chi_{\mathbf{h}} = -\frac{R\lambda^2}{\pi V} F_{\mathbf{h}} \quad (5)$$

where R is the classical radius of the electron, and V is the volume of a unit cell. $F_{\mathbf{h}}$ is the structure factor given by

$$F_{\mathbf{h}} = \sum_j (f_j + f'_j + if''_j) \exp(-M_j + i\mathbf{h} \cdot \mathbf{r}_j) \quad (6)$$

where f_j is the form factor of atom, and f'_j, f''_j are the anomalous dispersion correction. The exponent $\exp(-M_j)$ is the Debye-Waller factor.

The susceptibility due to the population inversion given by Eq. (3), mainly contributes to the anomalous uniform part of the susceptibility, which is denoted as $[\chi_{0,a}]_{m \rightarrow n}$. From Eq. (5) and (6), we can obtain the corresponding anomalous dispersion correction $(f'_j + if''_j)_{m \rightarrow n}$. Thus, as an approximation, the form factor plus the correction term can be substituted by

$$f_j + f'_j + if''_j \rightarrow f_j + (f'_j + if''_j)_{\text{gs}} + (f'_j + if''_j)_{m \rightarrow n} \quad (7)$$

where $(f'_j + if''_j)_{\text{gs}}$ takes the value of the anomalous correction of an atom in ground state. Therefore, the time- and space-dependent distribution of susceptibility is determined.

2.3 Time-dependent Takagi-Taupin equations

In a population-inverted crystal, the susceptibility is a spatial periodical function with time dependency, expanded in the Fourier series

$$\chi(\mathbf{r}, t) = \sum_{\mathbf{h}} \chi_{\mathbf{h}}(t) \exp(-i\mathbf{h} \cdot \mathbf{r}) \quad (8)$$

The properties of the electric field represented by the electric displacement vector $\mathbf{D}(\mathbf{r}, t)$ are described by the following wave propagation equation which is directly derived from the Maxwell equations

$$\nabla^2 \mathbf{D} + \nabla \times (\nabla \times \chi \mathbf{D}) - \frac{1}{c^2} \frac{\partial^2}{\partial t^2} \mathbf{D} = 0 \quad (9)$$

where c is the speed of light. The solution of Eq. (9) may be found in the form of an expansion of modulated waves [4]

$$\mathbf{D}(\mathbf{r}, t) = \sum_{\mathbf{h}} \mathbf{D}_{\mathbf{h}}(\mathbf{r}, t) \exp[i(\omega t - \mathbf{k}_h \cdot \mathbf{r})] \quad (10)$$

where $\mathbf{k}_h = \mathbf{k}_0 + \mathbf{h}$, and leads to a well known form of the Takagi-Taupin equations [4]. In the two-beam case, Eq. (10) reduces to the superposition of the incident and diffracted waves, which are denoted by the subscripts 0 and h in convention, respectively.

The Takagi-Taupin equations are originally proposed with the assumption that susceptibilities are constant in time. Since then, versions of modified Takagi-Taupin equations have been put forward to apply to the case of time-dependent susceptibility [5] as well as the case of crystals of arbitrary shape [6]. We here extend further the Takagi-Taupin equations to a more general case of an arbitrary shape of crystal with a time-dependent susceptibility. In this case we have for the modified Takagi-Taupin equations

$$\frac{\partial D_0}{\partial x_0} = -\frac{ik}{2} [\chi_0 D_0 + C \chi_h e^{i\Delta \mathbf{q} \cdot \mathbf{r}} D_h] - \frac{1}{c} \frac{\partial D_0}{\partial t} \quad (11a)$$

$$\frac{\partial D_h}{\partial x_h} = -\frac{ik}{2} [C \chi_h e^{-i\Delta \mathbf{q} \cdot \mathbf{r}} D_0 + \chi_0 D_h] - \frac{1}{c} \frac{\partial D_h}{\partial t} \quad (11b)$$

which are supplemented by the boundary conditions. Here the partial derivatives $\partial/\partial x_0$, $\partial/\partial x_h$ are taken along the directions of the wave vectors \mathbf{k}_0 and \mathbf{k}_h , and k is the magnitude of the wave vector in vacuum. Vector $\Delta \mathbf{q}$ represents the deviation from exact Bragg condition, which can be modeled as a small rotation of the crystal sample with constant incident and diffracted wave vectors $\mathbf{k}_0, \mathbf{k}_h$ [6]. When the crystal is rotated by a angle $\Delta\theta$, the end of the reciprocal lattice vector \mathbf{h} moves by $\Delta \mathbf{q} = \mathbf{h}' - \mathbf{h}$. In Eq. (11), C stands for the polarization factor, which is equal to unity in the case of a σ polarization and $\cos 2\theta_B$ in the case of a π polarization.

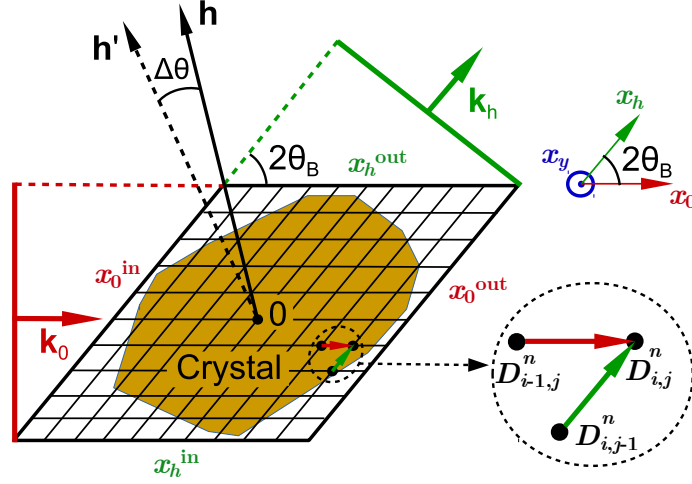


Figure 1: Schematics of the numerical model used for simulations of time-dependent Takagi-Taupin equations for a crystal of arbitrary shape. Crystal is rotated around the axis going through the crystal center that is perpendicular to the scattering plane defined by the vectors \mathbf{k}_0 and \mathbf{k}_h . The inset on the right shows recurrent relations for a single node of the grid.

In this paper we perform numerical integration of the Takagi-Taupin equations applying an approach similar to that described in Ref. [6]. To propagate the wave field along the directions of partial derivatives $\partial/\partial x_0$, $\partial/\partial x_h$, we introduce the laboratory coordinate system with the origin on the crystal rotation axis. The set of basis vectors $\{\mathbf{e}_0, \mathbf{e}_h, \mathbf{e}_y\}$ is represented by the unit vectors in the direction of the incident beam, diffracted beam, and normal to the scattering plane (see Figure 1). Thus, the partial derivatives are taken along \mathbf{e}_0 and \mathbf{e}_h vectors, and rotation is performed around the \mathbf{e}_y axis. The angle between the vectors \mathbf{e}_0 and \mathbf{e}_h is equal to $2\theta_B$, therefore the coordinate system generally is not orthogonal. Any position within the considered volume can be described by the radius vector $\mathbf{r} = x_0\mathbf{e}_0 + x_h\mathbf{e}_h + y\mathbf{e}_y$, where x_0, x_h, y are corresponding coordinates. We perform the numerical integration over a rhombic prism in which the whole crystal is embedded, as shown in Figure 1. More specifically, the prism is sliced to a set of layers, defined for different values of \mathbf{e}_y coordinate parallel to the scattering plane, and Takagi-Taupin equations are solved in the two-dimensional grid independently for each of these layers. Since directions $\mathbf{e}_{0,h}$ do not depend on the angular deviation $\Delta\theta$ in the chosen coordinate system the whole grid remains invariable during the angular scan, while rotation transformations are applied to the susceptibility of the crystal. The nodes, which belong to the crystal, are characterized by the values of Fourier components of the susceptibility, which are replaced by zeros for the nodes outside the crystal.

In the numerical integration method, the complex amplitudes $D_{0,h}(\mathbf{r})$ are represented by a discrete set of values over all of the integration grid and the Takagi-Taupin

equations are transformed to the following matrix form

$$\begin{pmatrix} D_{0;i,j}^n \\ D_{h;i,j}^n \end{pmatrix} = \mathcal{M} \begin{pmatrix} D_{0;i-1,j}^n \\ D_{0;i,j-1}^n \\ D_{0;i,j}^{n-1} \\ D_{h;i-1,j}^n \\ D_{h;i,j-1}^n \\ D_{h;i,j}^{n-1} \end{pmatrix}, \quad \begin{matrix} i = 1, \dots, N \\ j = 1, \dots, M \\ n = 1, \dots, L \end{matrix} \quad (12)$$

where the subscripts i, j represent the indexes of the spatial coordinates x_0, x_h , and the superscript denotes the index of the time coordinate. The coefficients of matrix \mathcal{M} are expressed as

$$\mathcal{M} = \frac{1}{A_{11}A_{12} - B_1B_2} \begin{pmatrix} A_{12}A_{21} & B_1B_2 & A_{12}E & -A_{12}B_1 & -A_{22}B_1 & -B_1E \\ -A_{21}B_2 & -A_{11}B_2 & -B_2E & B_1B_2 & A_{11}A_{22} & A_{11}E \end{pmatrix} \quad (13)$$

The parameters above are defined as

$$\begin{aligned} A_{11} &= 1 + \frac{ik\Delta x}{2} \frac{1}{2} [\chi_0]_{i-\frac{1}{2},j}^n + \frac{\Delta x}{c\Delta t}, & A_{21} &= 1 - \frac{ik\Delta x}{2} \frac{1}{2} [\chi_0]_{i-\frac{1}{2},j}^n \\ A_{12} &= 1 + \frac{ik\Delta x}{2} \frac{1}{2} [\chi_0]_{i,j-\frac{1}{2}}^n + \frac{\Delta x}{c\Delta t}, & A_{22} &= 1 - \frac{ik\Delta x}{2} \frac{1}{2} [\chi_0]_{i,j-\frac{1}{2}}^n \\ B_1 &= \frac{ik\Delta x}{2} \frac{1}{2} C [\chi'_h]_{i-\frac{1}{2},j}^n, & [\chi'_h]_{i-\frac{1}{2},j}^n &= \chi_{\bar{h}} \exp \left[i\Delta \mathbf{q} \cdot \left(x_0 - \frac{\Delta x}{2}, x_h \right) \right] \\ B_2 &= \frac{ik\Delta x}{2} \frac{1}{2} C [\chi'_h]_{i,j-\frac{1}{2}}^n, & [\chi'_h]_{i,j-\frac{1}{2}}^n &= \chi_h \exp \left[-i\Delta \mathbf{q} \cdot \left(x_0, x_h - \frac{\Delta x}{2} \right) \right] \\ E &= \frac{\Delta x}{c\Delta t} \end{aligned} \quad (14)$$

where Δx is the integration step for both directions, and Δt is the step for the time dimension.

From the numerical matrix form, we can see that for the spatial node (i, j) and time node n the values of amplitudes $D_{0,h;i,j}^n$ are calculated from the values $D_{0,h;i-1,j}^n$ and $D_{0,h;i,j-1}^n$ at the previous spatial nodes $(i-1, j)$ and $(i, j-1)$ and the current time node n , plus the values $D_{0,h;i,j}^{n-1}$ at the spatial node (i, j) and the previous time node n . In such a way calculations proceed from node to node in the direction of the transmitted and diffracted beams as well as the direction of time. The initial amplitudes of the incident and diffracted waves on each node are given by the initial conditions

$$D_0(\mathbf{r}, t=0), \quad D_h(\mathbf{r}, t=0) \quad (15)$$

The values of the amplitudes $D_{0,h}(\mathbf{r}, t)$ on the left and bottom boundary can be easily obtained

$$D_0(x_0=0) = D_0^{\text{in}}(x_h, t), \quad D_h(x_h=0) = 0 \quad (16)$$

The other two boundary conditions $D_0(x_h = 0)$ and $D_h(x_0 = 0)$ have to be determined via numerical method.

At $x_h = 0$, we have $D_h(x_h = 0) = 0$, and in result Eq. (11a) becomes

$$\frac{\partial D_0}{\partial x_0} = -\frac{ik}{2}\chi_0 D_0(\mathbf{r}, t) - \frac{1}{c}\frac{\partial D_0}{\partial t} \quad (17)$$

from which we can derive

$$D_{0;i,0}^n = \frac{1}{A_{11}} (A_{21}D_{0;i-1,0}^n + ED_{0;i,0}^{n-1}), \quad i = 1, \dots, N \quad (18)$$

where $D_{0;0,0}^n$ is given by D_0^{in} . Similarly, At $x_0 = 0$, we have $D_0(x_0 = 0) = 0$, and in result Eq. (11b) becomes

$$\frac{\partial D_h}{\partial x_h} = -\frac{ik}{2}[C\chi_h e^{-i\Delta\mathbf{q}\cdot(0,x_h)} D_0^{\text{in}} + \chi_0 D_h] - \frac{1}{c}\frac{\partial D_h}{\partial t} \quad (19)$$

from which we can derive

$$D_{h;0,j}^n = \frac{1}{A_{12}} \left[-B_2 \left(D_{0;0,j}^{\text{in};n} + D_{0;0,j-1}^{\text{in};n} \right) + A_{22}D_{h;0,j-1}^n + ED_{h;0,j}^{n-1} \right], \quad j = 1, \dots, M \quad (20)$$

where $D_{h;0,0}^n = 0$.

Once established these boundary conditions can be applied to any shape and orientation of the crystal embedded into the integration prism.

3 Results

3.1 The bench-marking calculations

In order to assure the correctness of the derived time-dependent Takagi-Taupin equations and the developed codes used for numerical calculation, we cross-check with the known simulation results given by Wark & Lee (1999) [5].

One of the simulations presented by Wark & Lee (1999) in Ref. [5] is carried out for the intensities of the incident and diffracted waves in unperturbed crystals. Figure 2 shows the depth-dependency of both the incident and diffracted intensities at a specific time for a crystal with a highly asymmetric rocking curve (Figure. 2(a)) and with a more symmetric rocking curve (Figure. 2(b)). It can clearly be seen that in the case of the asymmetric rocking curve, the incident wave effectively attenuates in the angular region near the Bragg condition due to the dynamical diffraction, while it penetrates deep into the crystal close to a particular angle out of the region of dynamical diffraction. On the other hand, for the more symmetric rocking curve, there is little penetration into the crystal for both the incident and diffracted waves.

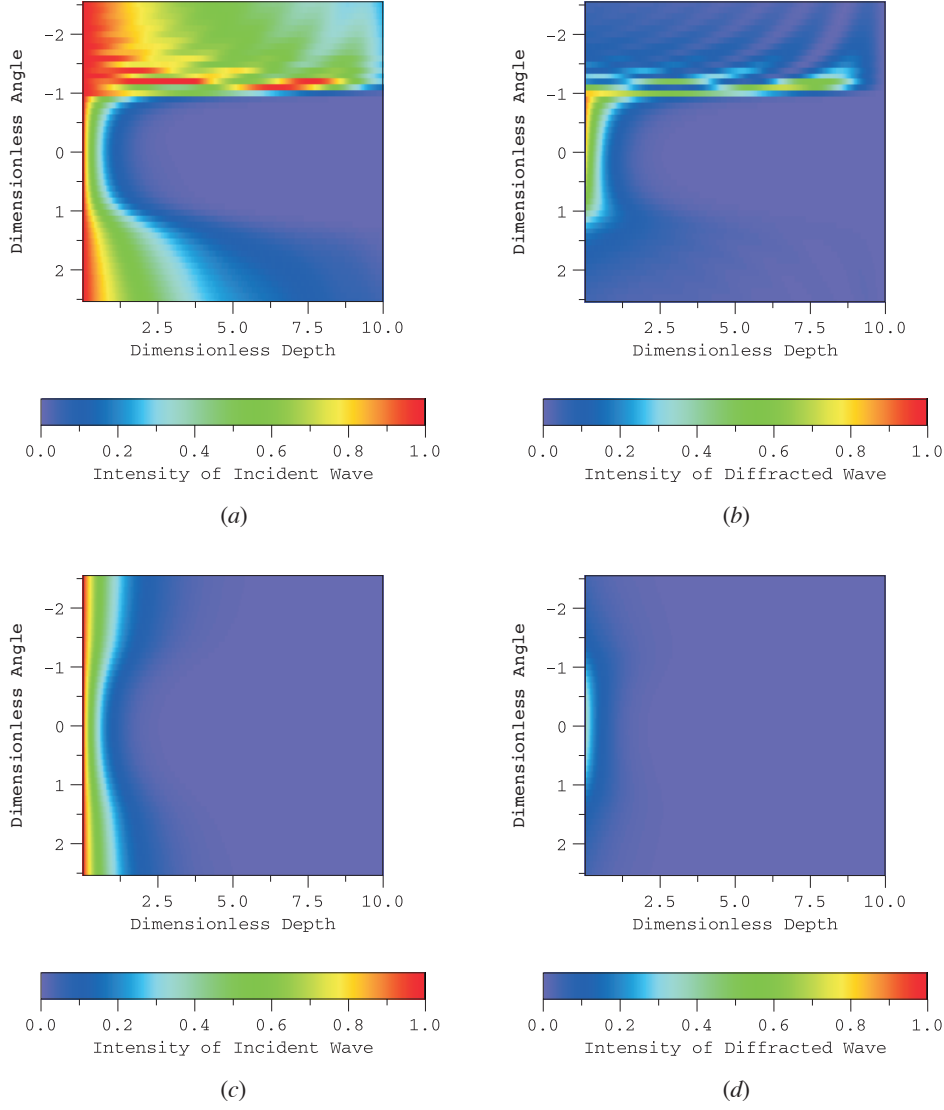


Figure 2: Depth- and angle-dependent intensity in the (a) incident wave and (b) diffracted wave for a crystal with a highly asymmetric rocking curve, and in (c) incident wave and (b) diffracted wave for a crystal with a symmetric rocking curve [5].

We repeat the simulations with the parameters in the Ref. [5] and successfully reproduced the numerical results. Figure 3 demonstrates the reproduction of Wark & Lee's simulations for the intensities of the incident and diffracted wave fields. Comparing Figure 2 and 3, it can be seen that our simulation results capture the essential features of the intensities of the wave fields shown in Figure 2, which can be regarded as a good criterion for the correctness of our modified equations and the codes. Note that the slight differences between the original results and the reproduced ones are due to the different units of the depth and the deviation angle adopted in the simulations.

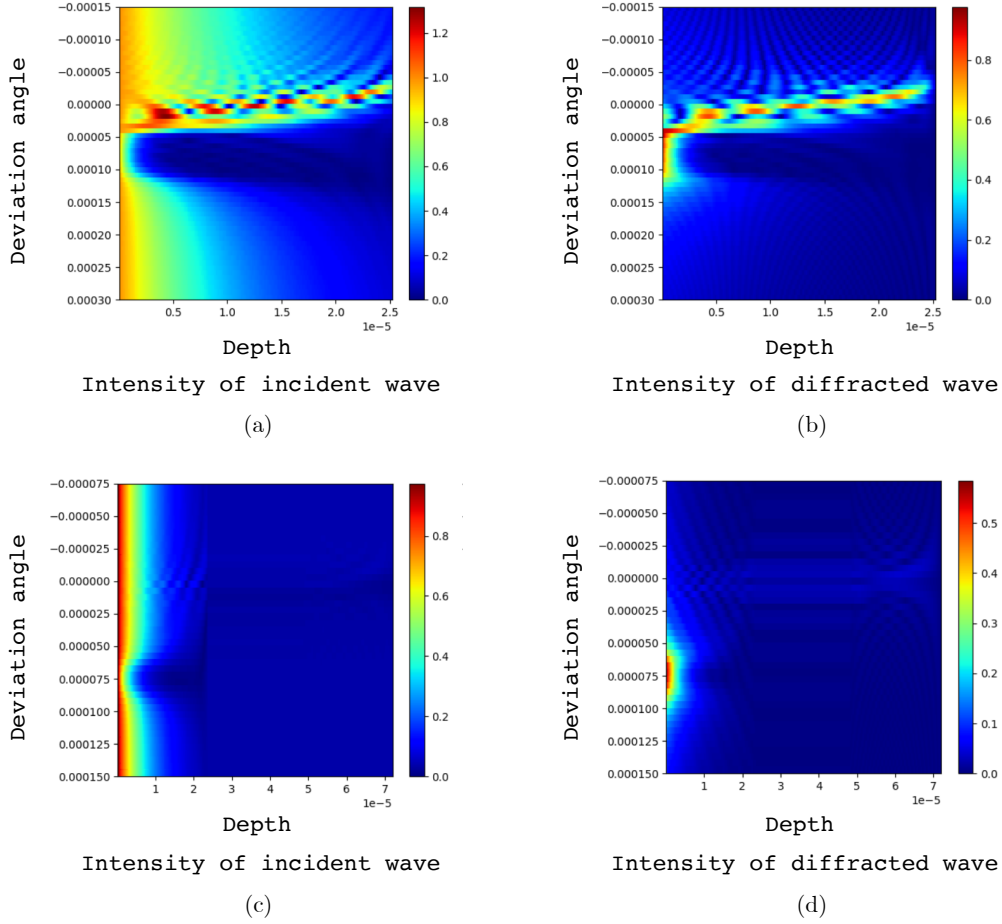


Figure 3: The reproduced depth- and angle-dependent intensity in the (a) incident wave and (b) diffracted wave for a crystal with a highly asymmetric rocking curve, and in (c) incident wave and (b) diffracted wave for a crystal with a symmetric rocking curve.

3.2 The population-inverted diffraction

Before simulating the population-inverted diffraction, we first present the simulations of the population inversion of Mn $K\alpha 1$ transition induced by an intensive pump pulse and calculate the corresponding x-ray susceptibility due to the coupling to the resonant population-inverted transition. We use a single-color Gaussian pulse tuned to the Mn K -absorption edge at photon energy of 6.6 keV for optical pumping. The pulse length is set to 14 fs with a temporal width of 7 fs at full-width at half-maximum (FWHM), and the spatial width (FWHM) is $1 \mu\text{m}$. The total number of photons in the pump pulse is about 1×10^{11} . The probe light overlapped with the pump pulse, is resonant to the Mn $K\alpha 1$ transition of 5.9 keV.

We focus our attention only on states $1s^{-1}$ and $2p^{-1}$, and plot the populations of the states and the population inversion as functions of time in Figure 4(a). We can see

that the population inversion takes place within $t = -6$ fs to 1 fs on the level of a few thousandths with a maximum of 0.007. After $t = 1$ fs, the upper state population is lesser than that of the lower state.

In Figure 4(b), we plot the time-dependent distribution of the x-ray susceptibility. It can be seen that the amplitude of the imaginary part of the susceptibility components χ_0 (red solid) is greatly enhanced (reaches a maximum about 3×10^{-4}) due to the resonance between the probe light and the Mn $K\alpha_1$ transition, the amplitude of imaginary part of $\chi_{h,\bar{h}}$ (purple solid) is also increased to a level of 10^{-5} . Moreover, the imaginary part of the χ_0 stays positive within the time region of population inversion, the positivity of which relates to the process of amplification, opposite to the normal attenuation of x-rays. Note that the real and imaginary parts of χ_h and $\chi_{\bar{h}}$ are the same.

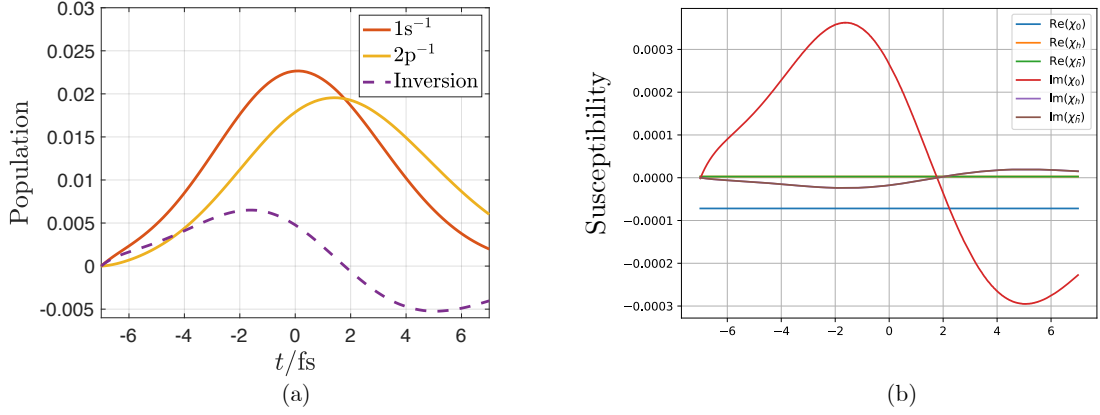


Figure 4: The time-dependent distributions of (a) the population of the states $1s^{-1}$ (red solid), $2p^{-1}$ (yellow solid) and the population inversion (purple dashed) and (b) the susceptibility of the resonant probe light.

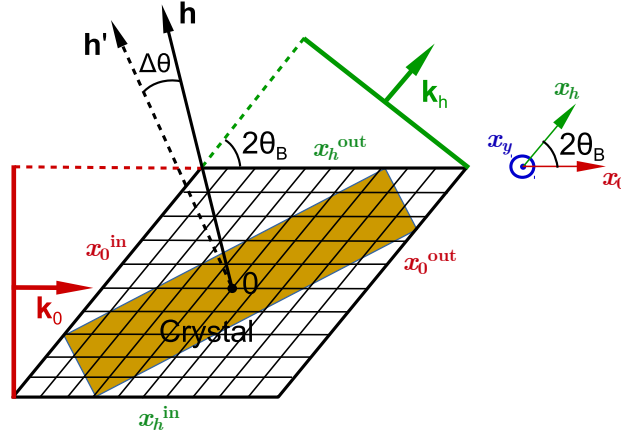


Figure 5: Diffraction geometry considered in simulations for an Mn crystal of a slab shape in real space. Red arrow indicates the incident beam and green arrow the diffracted beam. The reciprocal lattice vector \mathbf{h} is perpendicular to the surface of the crystal.

When the time-dependent susceptibility is obtained, the propagation of the incident wave (probe light) and the diffracted wave can be calculated based on the modified Takagi-Taupin equations. In order to illustrate general features of the diffraction in population-inverted medium, we consider a simple object in the form of Mn crystal in parallel-slab geometry without deformation. A schematics of the diffraction geometry in the real space and the nonorthogonal coordinate system with the x_0, x_h, y axes is shown in Figure 5. In our simulations we consider [400] reflection conditions and we strict ourselves to the geometry in which the reciprocal lattice vector \mathbf{h}_{400} is perpendicular to the surface of the crystal. The Bragg angle in these conditions is $\theta_B = 41.72^\circ$.

We perform simulations for three crystal sizes of 60 nm, 200 nm and 1000 nm at exact Bragg condition ($\Delta\theta = 0$). Figure 6 demonstrates the spatial distributions of the amplitudes of the incident and diffracted waves for the three crystals of different sizes. The small figures within each subgraph shows the spatial distribution of the wave fields at a specific time in the square integration plane which is transformed from the prism in the real space (see Figure 5). Note that the small figures are arranged in chronological order with time interval $\Delta t = 80$ fs.

In all of the cases, the incident waves are enhanced after their propagations in the crystals within the time region of population inversion, while undergo attenuation in the crystal after population inversion. The diffracted waves are increased as well in the population-inverted crystals.

Here we give an interpretation on the amplifications of the wave fields in the population-inverted medium based on analytical calculations. We now evaluate the extinction length L_{ex} which characterizes the decay of the incident wave when exact Bragg conditions are satisfied [6, 7], and the gain length l_{gain} . For sake of simplicity, we neglect the time derivative terms in Takagi-Taupin equations and estimate the static solution under the susceptibility at a specified time t . We shall strict ourselves to the slab geometry and assume that the dependence of the solutions along the surface can be neglected. The Takagi-Taupin equations can then be written as

$$\gamma_0 \frac{\partial E_0}{\partial z} = -\frac{ik}{2} [\chi_0 E_0 + C \chi_h E_h] \quad (21a)$$

$$\gamma_h \frac{\partial E_h}{\partial z} = -\frac{ik}{2} [C \chi_h E_0 + (\chi_0 - \alpha_h) E_h] \quad (21b)$$

where $\gamma_{0,h} = \mathbf{n} \cdot \mathbf{k}_{0,h}$ and \mathbf{n} is the inward normal to the entrance surface of the crystal, and α_h represents the deviation from Bragg condition [5]. For a perfect crystal without deformation, the intensity of the incident wave is [7]

$$\begin{aligned} I_0(z, \theta) &= I_0^{\text{in}} \exp \left\{ +\frac{2\pi\chi_{0,i}}{\gamma_0\lambda} z + \frac{2z}{L_{\text{ex}}} \text{Im}[C_2 R_0(\theta)] \right\} \\ &= I_0^{\text{in}} \exp \left\{ +\frac{1}{l_{\text{gain}}} z - \frac{2}{L_{\text{ex}}} \text{Im}[-C_2 R_0(\theta)] z \right\} \end{aligned} \quad (22)$$

We define the gain length and the extinction length as

$$l_{\text{gain}} = \frac{\gamma_0\lambda}{2\pi\chi_{0,i}}, \quad L_{\text{ex}} = \frac{\gamma_0\lambda}{\pi\sqrt{\beta}X_r} \quad (23)$$

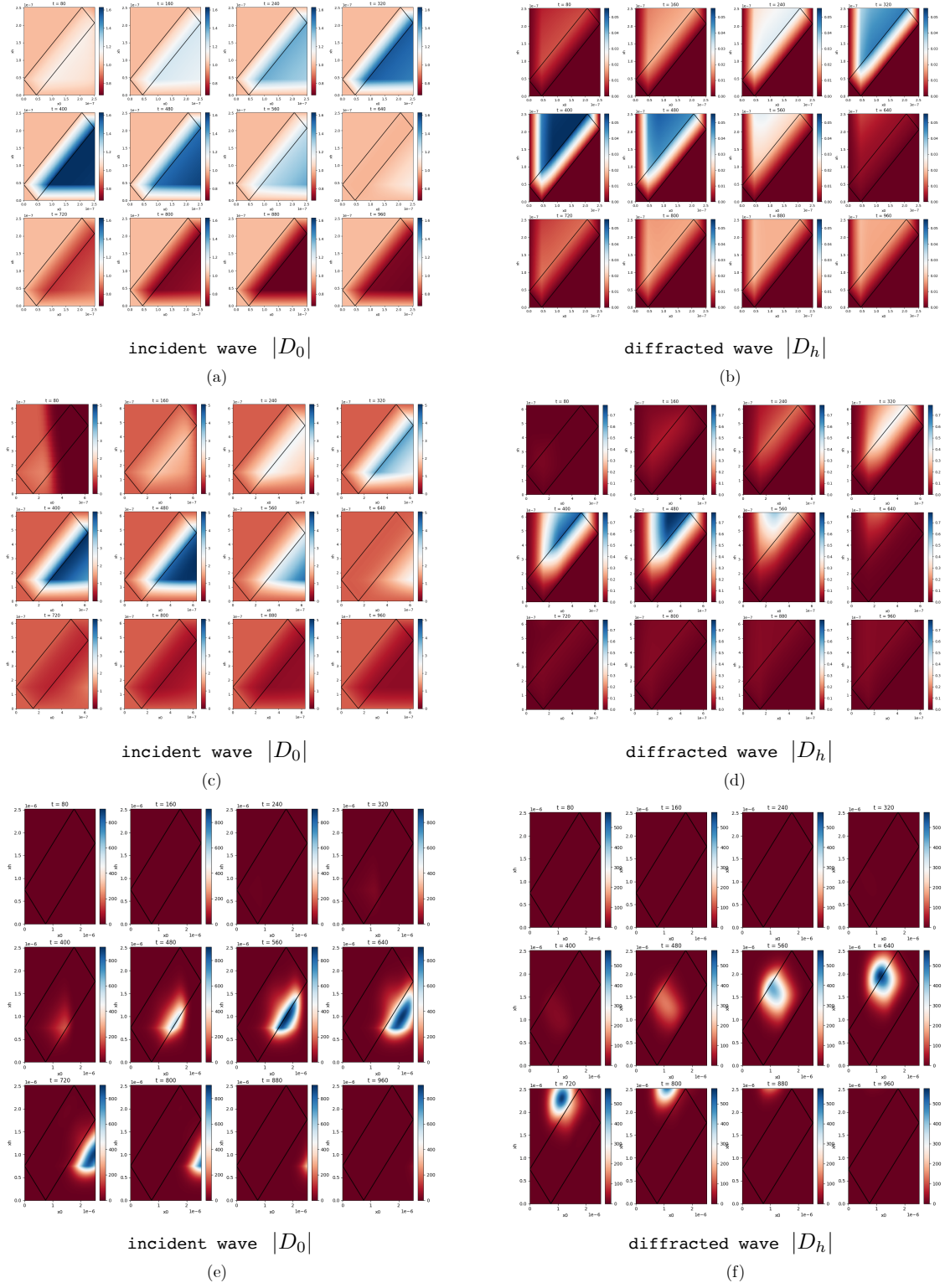


Figure 6: The spatial distribution of the amplitude of incident wave for the case of (a) 60 μm (c) 200 μm (e) 1000 μm thick crystal and the spatial distribution of the amplitude of diffracted wave for the case of (b) 60 μm (d) 200 μm (f) 1000 μm thick crystal. The boundary of the crystal is marked by black solid line. The small figures are arranged in chronological order with time interval $\Delta t = 80$ fs.

where

$$R_0(\theta) = \frac{1}{C_2} \left[-y(\theta) + \sqrt{y(\theta)^2 - C_2^2} \right] \quad (24)$$

$$y(\theta) = \sqrt{\beta} \frac{\sin 2\theta_B(\theta - \theta_B)}{X_r} + \frac{\chi_0(1 + \beta)}{2\sqrt{\beta}X_r} \quad (25)$$

and

$$\beta = \left| \frac{\gamma_0}{\gamma_h} \right|, \quad X_r = \text{Re}\sqrt{\chi_h\chi_{\bar{h}}}, \quad C_2 = C \frac{\sqrt{\chi_h\chi_{\bar{h}}}}{X_r}$$

Eq. (22) takes into account the amplification of the x-rays out of the angular region of Bragg condition ($|y(\theta)| \gg 1$).

$$I_0(z, \theta) = I_0^{\text{in}} \exp \left\{ + \frac{1}{l_{\text{gain}}} z \right\} \quad (26)$$

It also shows that a dynamical “extinction” effect arising from the multiple scattering of x-rays on the atomic planes in the narrow angular region of Bragg condition may be observed. In the angular region near the Bragg condition, Eq. (22) gives

$$I(z, \theta) = I_0^{(\text{in})} \exp \left\{ + \frac{1}{l_{\text{gain}}} z - \frac{2}{L_{\text{ex}}} \text{Im}[-C_2 R_0(\theta)] z \right\} \quad (27)$$

The first term in the exponent leads to an amplification of the incident wave, while the second term depicts an extinction as the Bragg condition is approximately satisfied. From Eq. (22)-(25), we see that l_{gain} is dependent on the susceptibility, and the extinction effect is modified by the deviation from the Bragg condition and the susceptibility at time t as well.

We define the effective extinction length as

$$L_{\text{eff}} = \left\{ \frac{2}{L_{\text{ex}}} \text{Im}[-C_2 R_0(\theta)] - \frac{1}{l_{\text{gain}}} \right\}^{-1} \quad (28)$$

and we have

$$I_0(z, \theta) = I_0^{(\text{in})} \exp \left(- \frac{z}{L_{\text{eff}}} \right) \quad (29)$$

If $L_{\text{eff}} > 0$, the incident wave attenuates during its propagation in the crystal due to the dynamical extinction effect, and no amplification of the beam can be observed. In its turn, if $L_{\text{eff}} < 0$, the incident wave is amplified as it travels through the crystal, while no extinction effect can be seen.

Figure 7 shows the characteristic lengths for the probe light of 5.9 keV inside the population-inverted crystal. We find that the modified extinction length is much greater than the gain length in most of the time, as a result $L_{\text{eff}} \simeq -l_{\text{gain}}$. We have $L_{\text{eff}} < 0$ within the time region of population inversion, which means that the dynamical extinction can not be observed but only the amplification at a maximum gain length of 70 nm, and have $L_{\text{eff}} > 0$ after the population inversion, indicating that the incident wave

undergoes attenuation in the crystal. This conclusion is in accordance with the numerical simulation of time-dependent Takagi-Taupin equations shown in Figure 6.

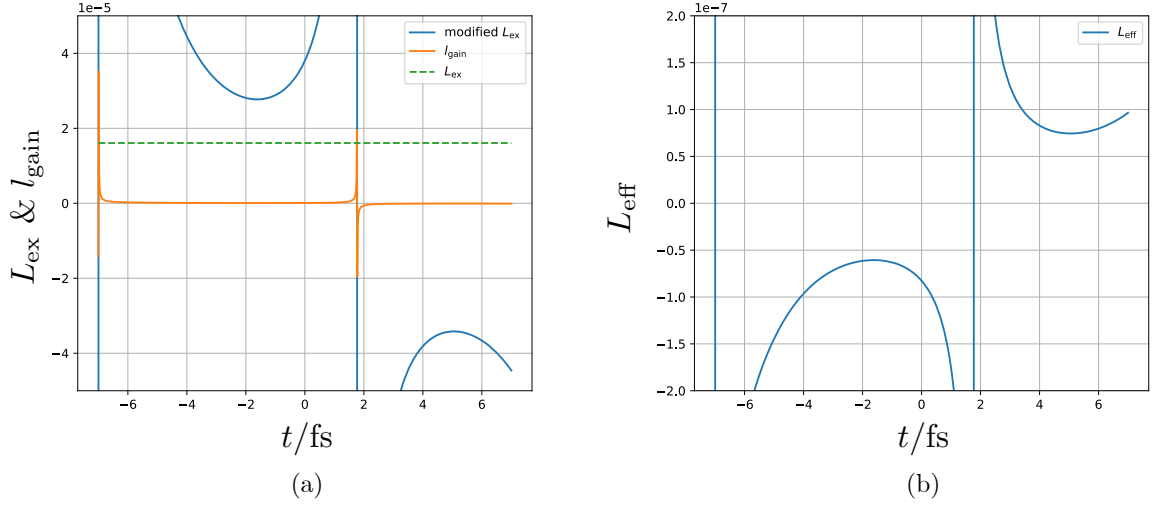


Figure 7: (a) The extinction length (green dashed), modified extinction length (blue solid), the gain length (orange solid) and (b) the effective extinction length as functions of time. The negativity of l_{gain} means the normal attenuation of x-rays in the crystal, while the negativity of the modified L_{ex} reflects an amplification effect due to the dynamical diffraction.

The analytical calculations show that the dynamical extinction is totally suppressed by the intensive amplification effect related to the positive $\chi_{0,i}$ caused by the population inversion. Even in our case, the kinematical approximation can be effectively applied to the diffraction problem. However, it should be noted that the conclusion that dynamical effects can be neglected should be quite specific for the parameters we have chosen. This conclusion can only give an interpretation on the numerical results of a special case of population-inverted diffraction and should not be a general conclusion.

4 Summary

To sum up, we have presented numerical model based on a modified form of time-dependent Takagi-Taupin equations and with the aim to study the dynamical effects for diffraction from population-inverted crystal of an arbitrary shape. To prepare the population-inverted medium, we have numerically simulated the population inversion of the Mn $K\alpha 1$ transition which reaches a maximum value of 0.007, and have calculated the x-ray susceptibility for the resonant probe light. As a result, the spatial distributions of the amplitudes of incident and diffracted waves have been calculated. We have also provided an interpretation on the amplification of the wave fields after its propagation in the crystal based on the analytical calculations we performed. We have reached on a conclusion that the dynamical effects can be neglected in the population-inverted

medium for the specific parameter in our case, which should not be a general conclusion. And we will focus on demonstrating the dynamical effects for diffractions from population-inverted crystal and determine the critical size of crystal below which the kinematical approximation can be applied in the later studies.

References

- [1] Sang-Kil Son, Linda Young, and Robin Santra. Impact of hollow-atom formation on coherent x-ray scattering at high intensity. *Phys. Rev. A*, 83:033402, Mar 2011.
- [2] Nina Rohringer and Robin Santra. X-ray nonlinear optical processes using a self-amplified spontaneous emission free-electron laser. *Phys. Rev. A*, 76:033416, Sep 2007.
- [3] Robert W. Boyd. *Nonlinear Optics*. Academic Press, 4 edition, 2020.
- [4] André Authier. *Dynamical Theory of X-Ray Diffraction*. Iucr Crystallographic Symposia. Oxford University Press, USA, 1 edition, 2001.
- [5] J. S. Wark and R. W. Lee. Simulations of femtosecond X-ray diffraction from unperturbed and rapidly heated single crystals. *Journal of Applied Crystallography*, 32(4):692–703, Aug 1999.
- [6] A. G. Shabalin, O. M. Yefanov, V. L. Nosik, V. A. Bushuev, and I. A. Vartanyants. Dynamical effects in bragg coherent x-ray diffraction imaging of finite crystals. *Phys. Rev. B*, 96:064111, Aug 2017.
- [7] I A Vartanyants and M V Kovalchuk. Theory and applications of x-ray standing waves in real crystals. *Reports on Progress in Physics*, 64(9):1009–1084, aug 2001.